AJNR

Experimental MR Imaging–guided Interstitial Cryotherapy of the Brain

Josef Tacke, Ralf Speetzen, Gerhard Adam, Bernd Sellhaus, Arndt Glowinski, Ingo Heschel, Tobias Schäffter, Robert Schorn, Stefanie Großkortenhaus, Günter Rau and Rolf W. Günther

AJNR Am J Neuroradiol 2001, 22 (3) 431-440
http://www.ajnr.org/content/22/3/431

AJNR Am J Neuroradiol 22:431–440, March 2001

Experimental MR Imaging–guided Interstitial Cryotherapy of the Brain

Josef Tacke, Ralf Speetzen, Gerhard Adam, Bernd Sellhaus, Arndt Glowinski, Ingo Heschel, Tobias Schäffter, Robert Schorn, Stefanie Großkortenhaus, Günter Rau, and Rolf W. Günther

BACKGROUND AND PURPOSE: **Hyperthermal ablation techniques such as laser or RF ablation require dedicated heat-sensitive MR imaging sequences for monitoring MR imaging–guided interventions. Because cryotherapy does not have these limitations, the purpose of this study was to evaluate the feasibility of MR imaging–guided percutaneous cryotherapy of the brain.**

METHODS: **An experimental cryoprobe with an outer diameter of 2.7 mm was inserted into the right frontal lobe of 11 healthy pigs under MR imaging control. Freezing procedures were monitored by using an interventional 1.5-T magnet and a gradient-echo sequence with radial k-space trajectories, a fast T2-weighted single-shot spin-echo sequence, and a T1-weighted single-shot gradient-echo sequence. In three animals, the procedure was also monitored by using dynamic CT. A freeze-thaw cycle with a duration of 3 minutes was repeated three times per animal. Follow-up MR images were obtained 3, 7, and 14 days after cryotherapy by using conventional MR sequences. Six animals were killed 7 days after intervention, and five animals were killed 14 days after intervention. The brains were sectioned, and the histologic findings of the lesions were compared with the MR imaging appearance.**

RESULTS: **No artifacts due to the probe were observed on the MR images or CT scans. The ice formation (mean diameter, 12.5 mm) was very well delineated as a signal-free sphere. MR monitoring of the freezing procedure yielded a significantly higher ice:tissue contrast than did CT. The size of the ice ball as imaged by MR imaging and CT during the intervention correlated well with the MR imaging appearance of the lesions at the 14-day follow-up examination and with the histologic findings. Histologically, coagulation necrosis and gliosis were found, surrounded by a transition zone of edema and a disrupted blood-brain barrier, corresponding to a contrast-enhancing rim around the lesions on follow-up MR images.**

CONCLUSION: **MR imaging–guided cryotherapy of the brain is possible and allows a precise prediction of the resulting necrosis. MR imaging of the freezing process does not require heat-sensitive sequences and is superior to CT for monitoring of cryoablation.**

Interventional MR imaging is a new and continuously growing field. During the past decade, different techniques have been developed, combining excellent soft-tissue contrast and multiplanar imaging capabilities with minimally invasive diagnostic and therapeutic techniques (1). During the past few years, different MR imaging–guided tissue ablation techniques have been developed, and some of them (ie, the hyperthermal ablation techniques) have achieved clinical application (2, 3). Others, such as focused sonography (4, 5), have been shown to be effective but are still experimental and depend on further technical development. A common problem of all hyperthermal ablation techniques is the imaging of temperature changes during heating the brain lesion. Although MR imaging principally indicates temperature changes, dedicated temperature-sensitive software and hardware are required to visualize the true extension of tissue damage. Furthermore, pulse sequences that exploit the temperature dependency of the resonance frequency of spins are extremely sensitive to motion.

Cryotherapy, which is still experimental in the field of interventional MR imaging (6), does not have these limitations. Because of an extreme de-

A.G., R.Sc., S.G., R.W.G.) and Neuropathology (B.S.) and the Helmholtz-Institute for Biomedical Engineering (R.Sp., I.H., G.R.), University of Technology, Aachen, Germany, and Philips Research Laboratories (T.S.), Hamburg, Germany.

This study was supported by a grant (TA 238–1) from the Deutsche Forschungsgemeinschaft.

Address reprint requests to Josef Tacke, MD, Department of Diagnostic Radiology, University of Technology, Aachen, Pauwelsstr. 30, 52057 Aachen, Germany.

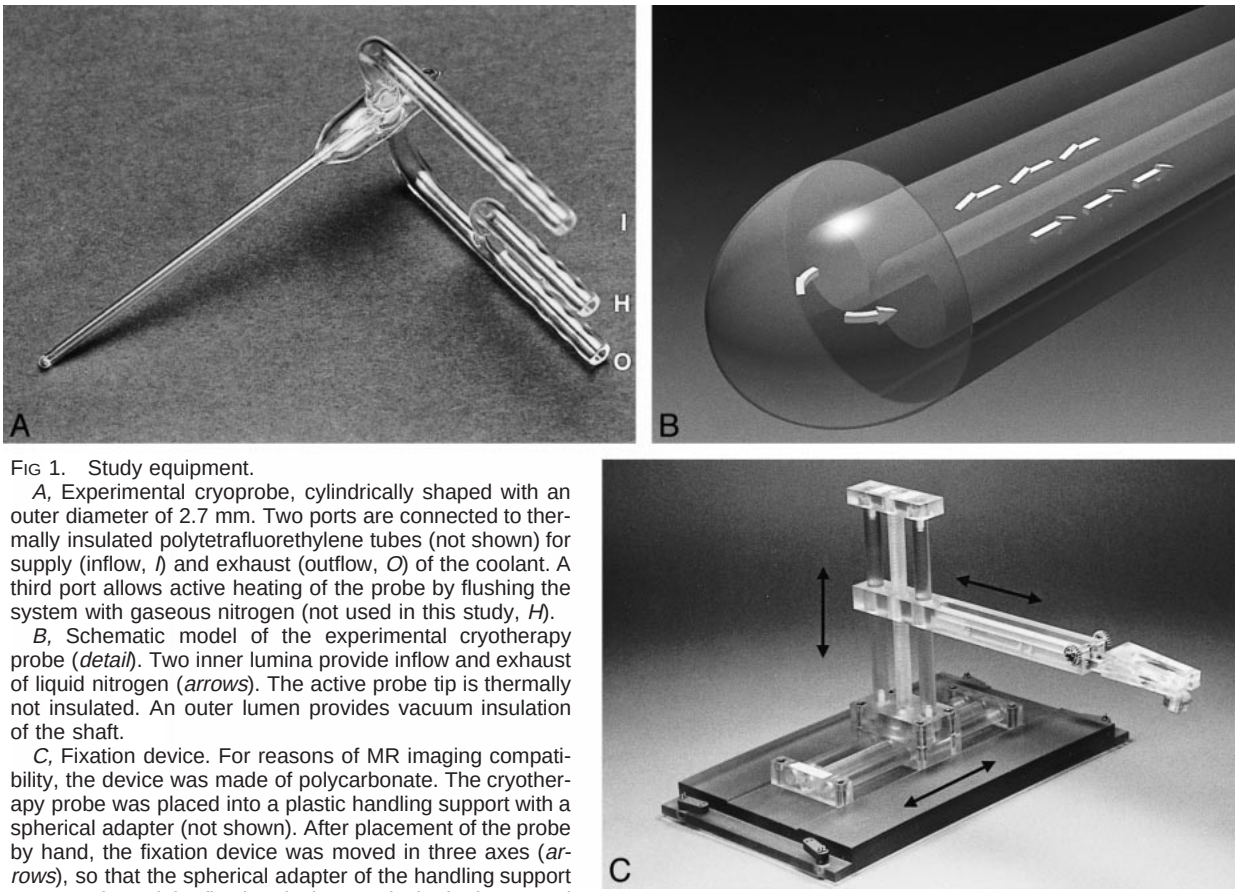

FIG 1. Study equipment.

A, Experimental cryoprobe, cylindrically shaped with an outer diameter of 2.7 mm. Two ports are connected to thermally insulated polytetrafluorethylene tubes (not shown) for supply (inflow, *I*) and exhaust (outflow, *O*) of the coolant. A third port allows active heating of the probe by flushing the system with gaseous nitrogen (not used in this study, *H*).

B, Schematic model of the experimental cryotherapy probe (*detail*). Two inner lumina provide inflow and exhaust of liquid nitrogen (*arrows*). The active probe tip is thermally not insulated. An outer lumen provides vacuum insulation of the shaft.

C, Fixation device. For reasons of MR imaging compatibility, the device was made of polycarbonate. The cryotherapy probe was placed into a plastic handling support with a spherical adapter (not shown). After placement of the probe by hand, the fixation device was moved in three axes (*arrows*), so that the spherical adapter of the handling support was caught and the fixation device was locked. The ground platter of the fixation device was locked on the MR imaging table before fixation of the probe.

crease of the T2- and T1-weighted TR, frozen tissue appears nearly signal-free on conventional MR images (7–9). Moreover, in recent experimental studies, it has been shown that there is a high correlation in lesion size between the ice as imaged by MR imaging and the histopathologic extension of the cryotherapy-induced lesion in glands such as the liver (10) or prostate (11). Until now, only one study of MR imaging–monitored cryotherapy of the brain has been published (6). It was performed with an experimental surface probe in rabbit brains and showed the feasibility of MR monitoring during cerebral cryotherapy. A previous, preliminary study showed that experimental interstitial cryotherapy of the brain by use of real-time MR imaging guidance is possible (12). The purpose of this study was to perform minimally invasive interstitial cryotherapy of the brain under MR imaging control, to monitor the freezing by different ultra-fast sequences including CT, to evaluate the imaging characteristics, and to correlate the histologic outcome after a follow-up period of 2 weeks with the initially frozen region.

Methods

Cryotherapy Device

The study was performed using an experimental MR imaging–compatible cylindrical probe with an outer diameter of 2.7 mm (Fig 1A). For reasons of MR imaging compatibility and resistance to the rapid drop of temperature, the probe was made of glass by a local glass manufacturer. The probe contained two inner lumina for inflow and outflow of the coolant and a surrounding lumen, providing vacuum insulation of the probe shaft except at the tip (Fig 1B). The active (ie, noninsulated) probe tip had a length of 3 mm. The probe was connected to two thermally insulated polytetrafluorethylene tubes. One tube was connected to a commercially available liquid nitrogen source, and the second tube provided the outflow of the mixture of liquid and gaseous nitrogen after passing the active probe tip. The effluent was collected in a closed discharge receptacle. The polytetrafluorethylene tubes had to be long because the liquid nitrogen source and discharge receptacle had to be kept outside the 5-gauss line of the main magnet field. To avoid loss of the cooling capacity, a bypass valve was placed between the supply tube and the exhaust tube 50 centimeters in front of the cryoprobe. The system pressure of the cooling device was 5 bars. The cryoprobe was designed at a 90-degree angle between the polytetrafluorethylene tubes and the probe shaft, because the direction of the insertion into the animal brain was perpendicular to B_0 and the space within the magnet bore was limited. The probe was held in place by a custom-made fixation device that allowed the operator to fix the probe at any desired position (Fig 1C). The freezing procedure was performed by three ''freeze-thaw'' cycles of 3 minutes' duration each.

Animal Model

The study was conducted in 11 male farm pigs (Deutsches Edelschwein) with a mean body weight of 40 kg. The study

was approved by our institution's Animal Care Committee. All interventions and follow-up controls were performed with the animals under general anesthesia. This was induced by intramuscular injection of 0.4 mg/kg atropine sulfate (WDT, Garbsen, Germany), 8 mg/kg azoperon (Stresnil; Janssen, Neuss, Germany), and 14 mg/kg ketamine hydrochloride (Ketamin, Sanofi, Düsseldorf, Germany). General anesthesia was maintained by IV injection of 1 to 2 mL of a 53 mg/mL pentobarbital sodium-containing solution (Narcoren, Rhone Merieux, Laupheim, Germany) through an 18-gauge canula into an ear vein. Finally, the animals were intubated and ventilated by a mixture of room air, oxygen, and carbon dioxide. The animals were placed on the imaging table in prone position with their feet first, and a flexible surface coil was fixed on the skull. After planning the intervention by multiplanar T2-weighted spin-echo imaging, a 5-mm osteotomy was placed in the region of the right frontal lobe under sterile conditions. The dura mater was slit, and the sterilized cryoprobe was gently inserted into the center of the right frontal lobe at a depth of approximately 2 centimeters from the surface. To avoid air-related susceptibility artifacts at the insertion site, a few drops of sterile saline were administered into the wound. After freezing, the probe was removed and the wound was closed by a single suture. Postoperatively, the animals received 4 mL of prednisolone (Prednisolon, 25 mg/mL; Albrecht, Aulendorf, Germany), 2.5 mL of metamizol natrium (Novaminsulfon, 500 mg/mL; Albrecht), 3 mL of Tardomycel (60,000 IU of benzylpenicillin-benzathine, 15,000 IU of benzylpenicillineprocaine, and 76 mg of dihydrostreptomycin per mL; BayerVital, Leverkusen, Germany) by subcutaneous injection. After extubation, the animals were allowed to recover for 3 days. Follow-up MR imaging was performed with the animals under general anesthesia 3 and 6 days after intervention in all animals and additionally after 14 days in five animals. The animals were then killed by an overdose of pentobarbital during injection of 10% buffered formalin into the right common carotid artery. The brains were sectioned, fixated in 10% buffered formalin for 4 weeks, and stained with hematoxylin and eosin for histologic evaluation.

MR System and Sequences

The study was performed using an interventional 1.5-T magnet (ACS-NT Gyroscan; Philips, Best, The Netherlands) and a receive-only surface coil with a diameter of 15 cm. The system is equipped with a floating table, allowing the operator to move the table easily in and out of the magnet bore. In-room monitors beside the magnet are used to view the images. The planning of the approach to the frontal lobe was performed by a T2-weighted turbo spin-echo sequence (1100/100 [TR/TE]; echo train length, 15; matrix, 254 × 256; field of view, 230/1.2; rectangular field of view, 80%; section thickness, 3 mm; imaging time, 1.25 minutes) in axial, sagittal, and coronal orientations. Because it was one aim of this study to evaluate the capabilities of modern fast imaging sequences for monitoring of the freezing, three different interventional sequences were used instead of conventional pulse sequences. For imaging of the first freezing cycle, a dynamic T1-weighted gradient-echo sequence (fast field echo) with a prepulse (16/6; flip angle, 20 degrees; inversion time, 100 ms; number of acquisitions, four; field of view, 170 mm; rectangular field of view, 55%; matrix, 179 × 256 matrix; section thickness, 5 mm; imaging time, 4 s per image) was used. The second freezing cycle was imaged using a dynamic single shot T2-weighted turbo spin-echo sequence (800/77; field of view, 280; rectangular field of view, 30%; echo train length, 46; matrix, 512; number of acquisitions, one; imaging time, 440 ms per image) with the so-called zoom imaging or local look (LoLo) technique, characterized by a perpendicular orientation of the 180-degree pulse to the 90-degree pulse (13). Finally, a T1-weighted single shot gradient-echo sequence with radial k-space trajectories (10/4; flip angle, 50 degrees; section thickness, 5 mm; field of view, 300) was applied for imaging of the third freezing cycle. In the radial sequence, the image reconstruction was performed following the principle of the filtered back-projection (14) at an image rate of ≤25 frames per second with the ''sliding window'' technique (15). The speed of this sequence is related to only a part of the k-space profiles' being newly acquired for each reconstructed image, whereas the remaining k-space profiles are taken from the previously acquired data set. During every interleave of the radial k-space trajectories, one fourth of the newly acquired profiles are placed symmetrically in k-space. A completely new image is based on 352 radial profiles, and every profile is based on 256 points in k space. The current data set is transformed into an image by a special back projector, resulting in a real-time image update. An implemented software allows the operator to change interactively the flip angle, section thickness, orientation, and angulation during imaging. The continuously reconstructed images were recorded on a standard video recorder. To compare the monitoring capabilities of MR imaging with those of CT, the third freeze-thaw cycle of three animals was monitored by CT. Therefore, the entire experimental set-up, including the animals with the cryoprobe in situ, was moved carefully into the CT room. Dynamic scans of 5-mm thickness (290 mA, 120 kV) were obtained in coronal orientation by using a Somatom Plus scanner (Siemens, Erlangen, Germany).

Follow-up examinations included a multiplanar T2-weighted turbo spin-echo, fluid-attenuated inversion recovery sequence (6000/150; inversion time, 2000 ms; field of view, 190/1.5; rectangular field of view, 90%; echo train length, 25; matrix, 245 × 256; section thickness, 3 mm) and T1-weighted spin-echo sequences (550/257; field of view, 230/2; matrix, 205 × 256; section thickness, 3 mm) obtained before and after a bolus administration of 0.1 mmol/kg gadopentetate dimeglumine (Magnevist; Schering, Berlin, Germany) into an ear vein.

Data Analysis

The signal intensity was obtained from one region of interest within the ice formation and from another within the corresponding brain parenchyma of the contralateral frontal lobe on coronal views of MR images and CT scans. To evaluate the contrast difference between frozen and unfrozen brain for each sequence and to compare the ice appearance on MR images and CT scans, the values of unfrozen brain were standardized to 100 and the contrast difference was calculated in percent for each animal. The diameters of all lesions (ie, the appearance of the ice formation on the different MR sequences and CT scans, as well as the lesions on follow-up MR images) were measured in coronal and, if available, axial and sagittal orientations. They were correlated to the diameters of the lesions in the histologic specimens. Statistical evaluation was performed using the Wilcoxon test for unpaired samples and the unpaired *t* test. Significance was assumed if the *P* value was below .05.

Histologic Examination

After fixation in 10% buffered formalin, the brains were sectioned in coronal slices, and the largest diameters of the cryolesions were measured macroscopically using a ruler. A shrinkage factor of 1.14 of the histologic specimen, which occurs because of formalin fixation (16), was taken into account for data correlation. Specimens of the cryolesions, the surrounding tissue, and untreated areas of the cortex, basal ganglia, and brain stem were prepared for histologic examination and were stained with hematoxylin and eosin. The specimens were then stained with antibody against glial fibrillary acidic protein.

Results

MR imaging–guided cryotherapy was successfully performed in 11 animals. The percutaneous

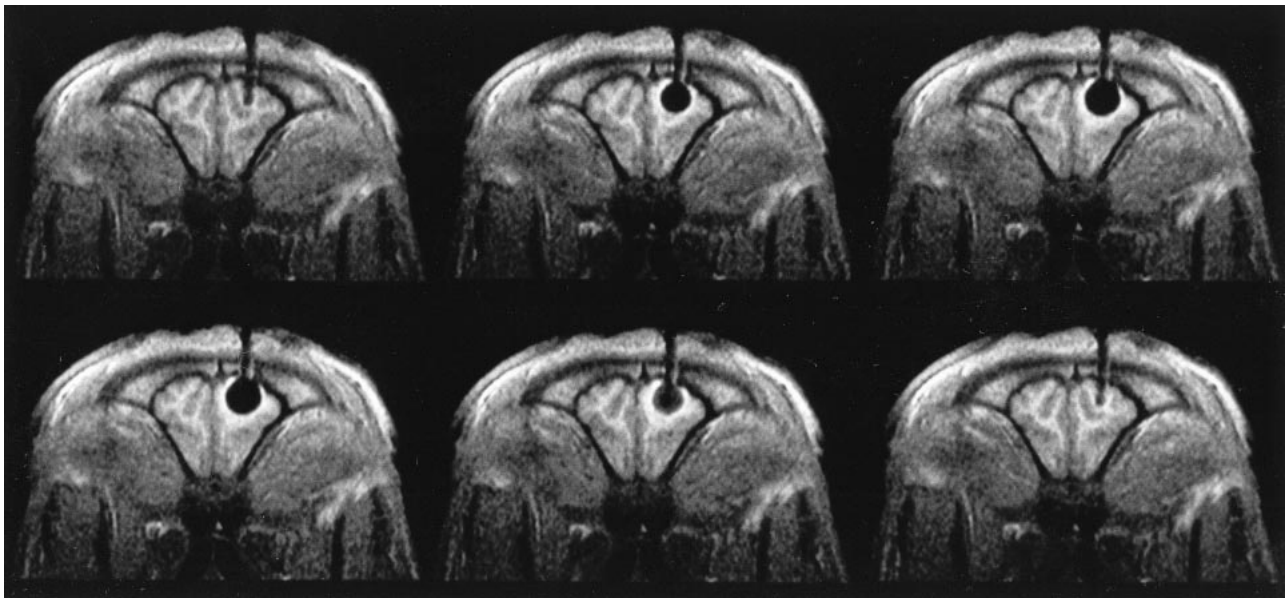

FIG 2. Dynamic T1-weighted fast field echo coronal section of the anterior brain, obtained during the first freezing cycle. The imaging duration was 4 seconds. The inactive cryoprobe appears signal free and causes no artifacts (*upper row, left*). After passing cryogen through the probe (from left to right), a signal-free and spherically shaped ice ball forms around the probe tip. Excellent ice:tissue contrast (91%, mean signal intensity of the ice, 90.7 ± 21.6; mean signal intensity of the unfrozen brain, 1032.5 ± 135.6). Note the hyperintense rim around the signal-free ice, which follows the growing and thawing ice formation and is assumed to represent the temperature gradient of the cooled but unfrozen tissue. Signal increase of the ice is seen during thawing (*lower row, middle*).

probe insertion was without complication, except in one case. In this animal, the slitting of the dura mater was insufficient, leading to an epidural hematoma after inserting the probe. This animal was excluded from the study. In the remaining animals, no complications occurred during placement of the probe within the frontal lobe or during the freezing procedure. Neither the cryoprobe nor the fixation apparatus caused any artifacts during MR imaging. On the MR images that were obtained to confirm the position of the uncooled probe, it was clearly visible as a hypointense ''tube'' in the normal intense brain (Figs 2–4). On CT scans, the cryoprobe appeared hyperdense and caused artifacts along the axis of the probe shaft (Fig 5) due to beam hardening of the probe and the fixation apparatus. During freezing, there was no visible ice formation along the insulated probe shaft. Further, no artifacts of flushing the probe with gaseous nitrogen during the cooling phase of the supplying tubes were observed. The ice around the probe tip was continuously observed and was clearly visible as a spherically shaped, signal-free area. The mean duration from starting the freezing procedure until achieving the maximum diameter was 1.5 minutes. The ice formation was sharply delineated and was surrounded by a thin rim of increased signal intensity on T1-weighted fast field echo images and radial fast field echo images (Figs 2 and 4). This signal increase was less clearly observed on T2-weighted LoLo sequences (Fig 3). Because they were continuously observed as a moving frontier between the unfrozen tissue and the ice from the beginning of freezing until the end of thawing, the signal changes were assumed to represent the temperature gradient of the cooled but unfrozen tissue (8). The maximum diameter of the ice ball increased during repetitive freezing from 11.7 ± 1.3 mm (mean value ± SD), to 11.9 ± 9 mm, to a final 12.4 ± 9 mm.

In all tested MR sequences, the ice:tissue contrast was sufficient and allowed a precise differentiation between the frozen and unfrozen brain tissue. It was best using the T1-weighted fast field echo sequence (91% ± 2.3%, compared with the opposite side). Using the radial fast-field echo sequence, this value was 89% ± 4.3%, and using the LoLo sequence, it was 81% ± 13.4%. Using coronal CT for monitoring the freezing process, the ice:tissue contrast was 58% ± 11.2%. The differences in ice:tissue contrast between the T1-weighted fast field echo sequence and the LoLo sequence were statistically significant ($P < .0098$) but not in comparison with the radial fast-field echo sequence. There were no statistically significant differences between the ice:tissue contrast using the LoLo and radial fast field echo sequences. The ice:tissue contrast of all tested MR imaging sequences was superior to that of coronal CT ($P < .001$).

The image acquisition time of all sequences including CT, ranging from 440 ms (LoLo) to 4 seconds (T1-weighted fast field echo), was sufficient in monitoring the freezing process, because the time course of ice growth was long enough compared with the image acquisition time. With respect to the multiplanar imaging capabilities of MR imaging, the radial fast field echo sequence (Fig 4) was superior to the T1-weighted fast field echo and LoLo sequences in that it allowed the operator to change the section orientation during imaging and

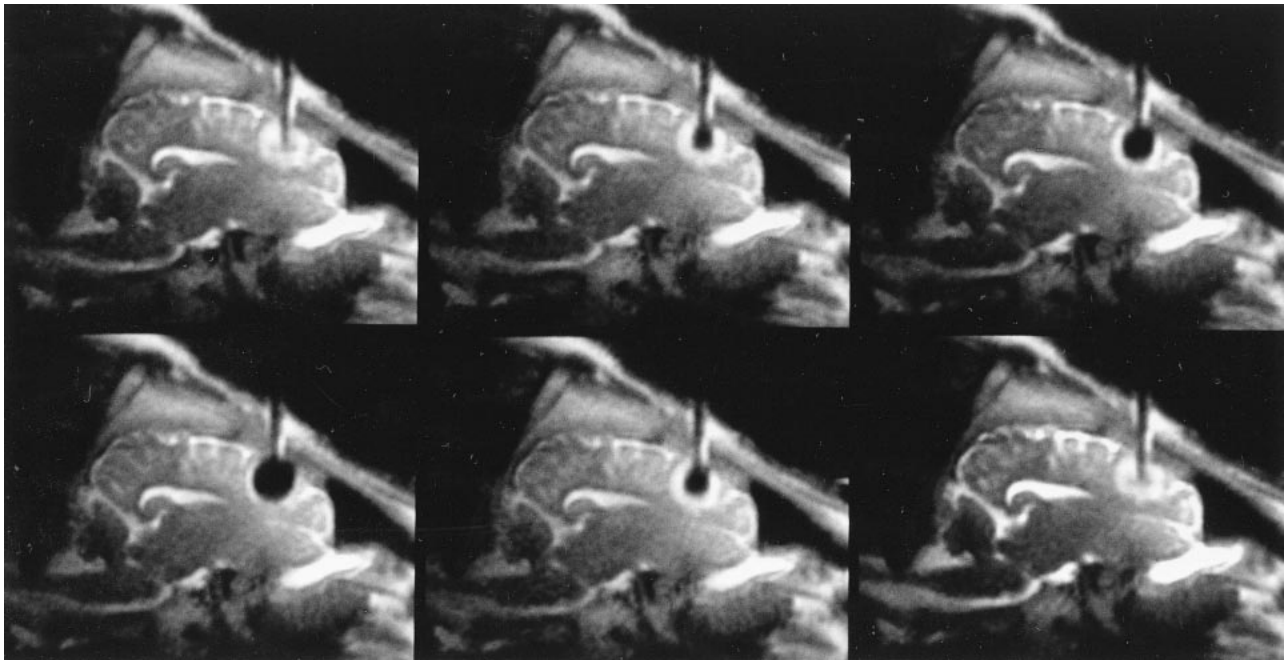

FIG 3. Dynamic T2-weighted LoLo sequence, sagittal plane through the right hemisphere, second freezing cycle. The imaging duration was 400 milliseconds. The cryoprobe appears as an artifact-free tubular structure. A spherically shaped zone of edema around the inactive probe tip after an initial freeze-thaw cycle can be seen. The T2-weighted contrast provides good delineation of the CSF. The ice:tissue contrast (81%, mean signal intensity of the ice, 240 ± 21.6; mean signal intensity of the unfrozen brain, 1313.4 ± 275.2) was not as good as that of the T1-weighted fast field echo sequence but was sufficient to distinguish ice from tissue.

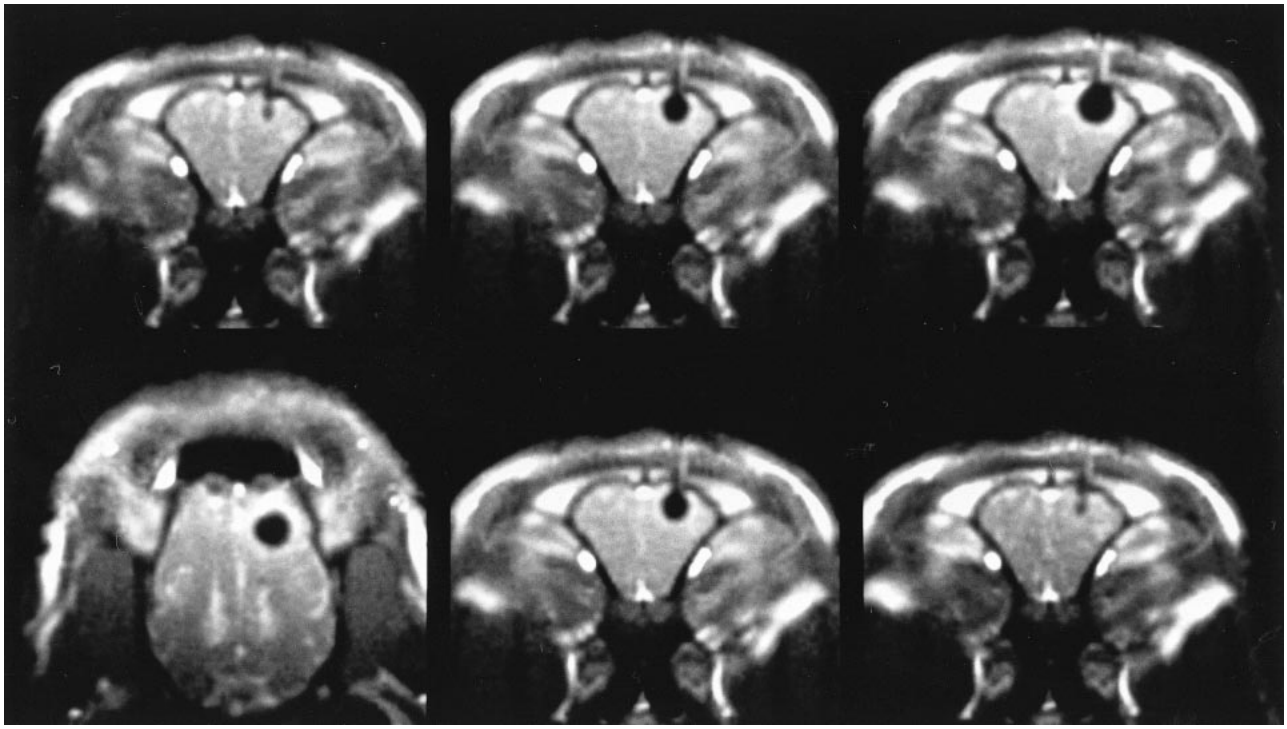

FIG 4. Multiplanar radial fast field echo image, obtained during the third freezing cycle. Fluoroscopic MR imaging with ≤25 images per second was performed. The appearance of the inactive and active probe, including the ice formation, comes close to that of T1-weighted fast field echo, although the spatial resolution is reduced. Excellent ice:tissue contrast (mean signal intensity of the ice, 50.9 ± 21.6; mean signal intensity of the unfrozen brain, 474 ± 107). Interactive change from coronal to axial plane during scanning is shown (*bottom row, left*). Bright contrast of vasculature, which is orthogonal to the imaging plane (venous sinuses and orbital veins), can be seen. The hyperintense halo around the ice is present but is less well seen than that on T1-weighted fast field echo images.

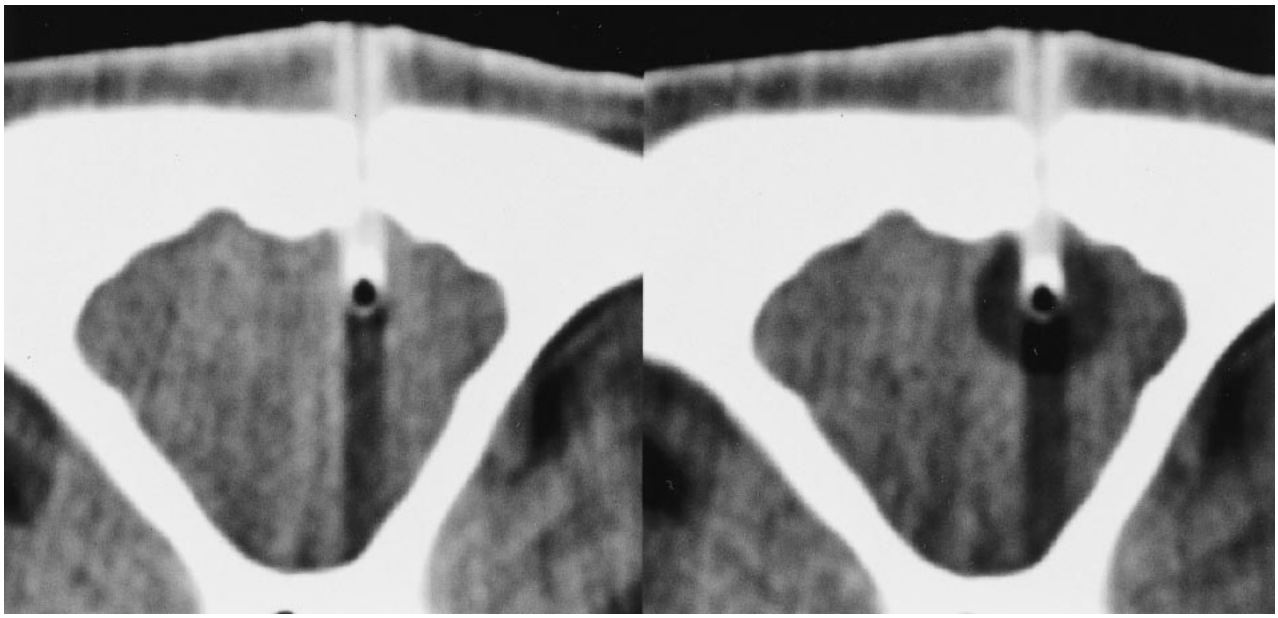

FIG 5. Coronal view, 5-mm section thickness, soft-tissue window CT scan. The scan duration was 1 second. The inactive probe (*left*) was hyperdense, except at the tip (active tip without vacuum insulation) and caused no relevant artifacts. Stripe-shaped artifacts due to the cryotherapy probe and the fixation device can be seen. The ice (*right*) appears as a spherically shaped, sharply delineated hypodense formation around the probe tip. Although the density of the frozen brain (mean, -23.7 ± 15.6 Hounsfield units) is clearly differentiable from that of the unfrozen brain (mean, 32.5 ± 3.2 Hounsfield units), the ice:tissue contrast is statistically significantly inferior to that of all MR images (58%, $P < .001$).

thus allowed complete imaging of the ice extension in all spatial dimensions.

MR images of the brain obtained immediately and at 3, 7, and 14 days after cryotherapy showed spherically shaped lesions of different sizes and appearances. Immediately after the freezing, the cryolesions were isointense to the adjacent brain tissue but were surrounded by a hyperintense edematous ring on T2-weighted sequences (Fig 6A). On fluid-attenuated inversion recovery images, a beginning edema surrounding the cryolesion was observed. On contrast-enhanced T1-weighted images, the lesions were isointense to the adjacent brain but surrounded by a thin, contrast-enhanced rim, representing a disruption of the blood-brain barrier. The size of the ice ball and the lesion extensions were in good accordance. No statistically significant difference was observed. Three days after the intervention, the center of the lesions turned into an inhomogeneous hyperintense signal, and the diameter of the lesions increased to nearly 135% on T2-weighted images as compared with the initial size of the ice ball. On fluid-attenuated inversion recovery images, the lesions were embedded in an inhomogeneous and irregularly shaped zone of edema. The diameters of the cryolesions, including the total extension of the edema, increased to nearly 150% of their original size. On contrast-enhanced T1-weighted images, the diameters of the cryolesions, including the contrast-enhancing rim, increased slightly but not more than 15%. The increase of lesion size 3 days after cryotherapy was statistically significant for all sequences ($P < .04$). Seven days after cryotherapy, the size of the lesions decreased on T2-weighted images to 120%, as compared with the initial ice ball size (Fig 6B). A thin signal-free rim surrounding the hyperintense lesion was observed, representing a thin layer of hemosiderin. On fluid-attenuated inversion recovery images, the edema decreased slightly to 125%, as compared with the ice. On contrast-enhanced T1-weighted images, the diameter of the lesions, including the contrast-enhancing rim, decreased to 108%. The differences in size compared with the initial diameter of the ice ball were significant only for T2-weighted and fluid-attenuated inversion recovery sequences. Fourteen days after freezing, the lesions appeared homogeneously hyperintense on T2-weighted images and the ring of hemosiderin was seen more clearly (Fig 6C). On the fluid-attenuated inversion recovery images of most of the animals, the surrounding edema disappeared. On contrast-enhanced T1-weighted images, the lesions were sharply delineated by a thin rim of disrupted blood-brain barrier. Fourteen days after cryotherapy, no statistically significant difference in lesion size compared with the size of the initial ice ball was observed on fluid-attenuated inversion recovery, T2-weighted, or contrast-enhanced T1-weighted images.

Histology

The mean diameter of all cryolesions was 12.95 mm $\pm$ 1.33, after the shrinkage factor of 1.14 was taken into account (Fig 7A). There was no statistically significant difference in size comparing the mean diameters of the previously frozen brain

FIG 6. MR images of the brain obtained immediately and at 3, 7, and 14 days after cryotherapy showed spherically shaped lesions of different sizes and appearances.

A, Axial plane T2-weighted turbo spin-echo (*left*) and contrast-enhanced T1-weighted spin-echo (*right*) images obtained immediately after the freezing. A spherically shaped ring of edema around an isointense cryolesion is visible (*left*). On the contrast-enhanced image (*right*), the disrupted blood-brain barrier in the location of the previous interface of frozen and unfrozen brain tissue is visible. Hemorrhage within the lesion can be seen. An inactive cryoprobe is still left in situ.

B, Seven days after therapy, the cryolesion appears inhomogeneously hyperintense, surrounded by an inconstant thin rim of hemosiderin (*left*). Edema in the adjacent white matter can be seen. Thickening of the zone of the disrupted blood-brain barrier is visible on the contrast-enhanced image (*right*).

C, Fourteen days after cryotherapy, the cryolesion appears homogeneously hyperintense on the T2-weighted image (*left*). The rim of hemosiderin decreased further in signal intensity and surrounds the lesion entirely. The edema outside the cryolesion disappeared incompletely. After the administration contrast medium (*right*), the zone of disrupted blood-brain barrier decreased in thickness, enabling a sharp delineation of necrosis and viable brain tissue.

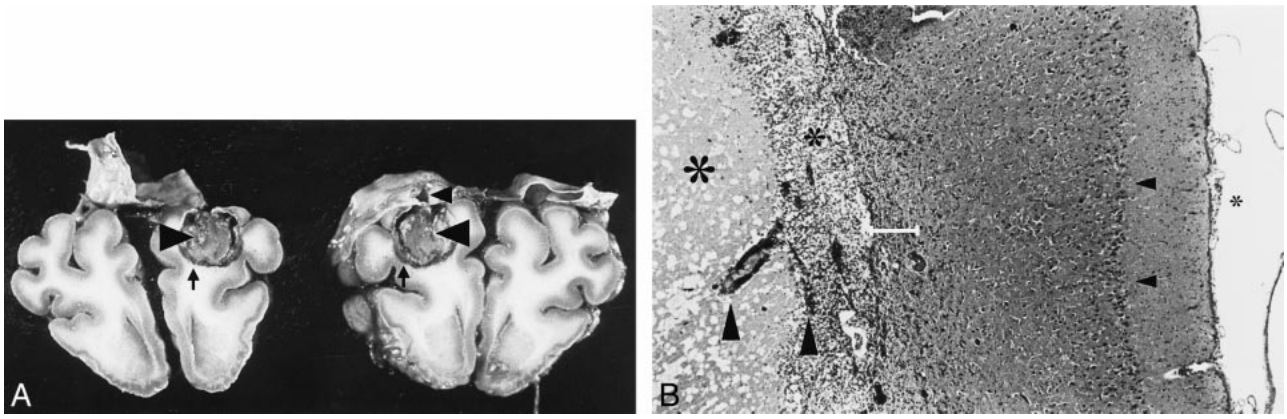

FIG 7. Histologic findings.

A, Gross view of one brain specimen after formalin fixation and coronal section. The lesion was dissected in the center. The frontal section on the *left* shows sharply delineated necrosis (*large arrowhead*) in the right hemisphere and a small rim of extravasated blood (*arrow*). The directly following parietal specimen on the *right* was turned over, so the same lesion is now seen on the *left.* Necrosis (*large arrowhead*) and rim of extravasated blood (*arrow*) are identical. Iatrogenic lesion of the dura mater (*small arrowhead*) is inconspicuous. Note the absence of general brain edema and severe hemorrhage.

B, Histologic detail of cryolesion and neighboring cortex. Meninges (*small asterisk*), cerebral cortex with neuronal layer (*small arrowhead*), and following subcortical white matter are seen above and are unaffected. Transition zone (*bar*) next to the lesion consisting of vital, edematously, and spongiously altered tissue. Neurons are damaged selectively, when they are involved. Many capillaries (*large arrowheads*) were observed sprouting from this area and leading into the outer zone of necrosis. In this outer zone (*medium asterisk*), numerous leukocytes and macrophages were seen. Neutrophils and lymphocytes were also present, in variable composition. In the center of the necrosis (*large asterisk*), amorphous necrotic tissue with corresponding paleness of nuclei, cell bodies, and fibers was observed (hematoxylin and eosin; original magnification, ×60).

tissue and the MR imaging appearance of the cryolesion immediately and at 7 and 14 days after cryotherapy.

Seven days after the initial cryotherapy, the coagulation necrosis was very well delineated from the adjacent unfrozen brain tissue. The previously unfrozen brain tissue showed an inconspicuous structure with normal and glial cells. Next to the necrosis, a transition zone 200 μm in diameter was observed (Fig 7B). This consisted of vital but edematously and spongiously altered tissue. Whereas several neurons were stained dark and obviously selectively structurally damaged, astrocytes and corresponding glial fibers were prominent.

Immunohistologic staining with antibody against glial fibrillary acidic protein reveals a medium degree of increasing expression. These tissue changes in the transition zone can be summarized as a surrounding area of gliosis in combination with partial and selective loss of neurons. Many capillaries were observed sprouting from this area and leading into the outer zone of the necrosis. In this outer zone, numerous leukocytes and macrophages were seen. Neutrophils and lymphocytes were also present in variable composition. Focally, a thin rim of extravasated blood was observed. This was several days old and obviously resulted from the initial cryotherapy. Hemoglobin was transferred to hemosiderin, and siderophages were present. Severe hemorrhage was absent. In the center of the necrosis, amorphous necrotic tissue with corresponding paleness of nuclei, cell bodies, fibers, and blood vessels was observed with hematoxylin and eosin staining.

Immigration of leukocytes was seen in small foci. In the 7-day-old cryolesions, the necrotic tissue was edematously swollen. Fourteen days after cryotherapy, the edema was decreasing. Within the necrosis, early cavitating stage with increased organization by macrophages, advanced capillarization, and absence of additional bleeding was seen.

Discussion

Tissue damaging by use of deep temperatures is pesumably the oldest technique of tissue ablation and has potential benefits over other, hyperthermal ablation techniques. First, no toxic or reactive byproducts are created during freezing or thawing of the target lesion. Second, the therapeutic effect is limited to the ice formation around an active cryotherapy probe. In opposition to hyperthermal techniques, the volume of damaged tissue does not increase after finishing the ablation procedure. Third, the scarring after cryoablation is minimal as known from ophthalmology and dermatology. Finally, and most importantly, the extension of the frozen tissue can be precisely controlled by imaging techniques such as sonography, CT, and MR imaging, because the transfer of tissue fluid from the liquid into the solid phase results in a different echogeneity, density, and relaxation time of frozen tissue (6–9).

Our study showed that MR imaging–guided minimal invasive cryotherapy of the brain is possible and allows precise predictability of the resulting size of tissue necrosis. The use of fast and ultrafast MR sequences enables optimal monitoring of the tissue damaging process with high temporal and spatial resolution.

Because of the excellent soft-tissue contrast of MR imaging, it is increasingly used for image-guided neurointerventions. Most frequently, monitoring with MR imaging is used for image-guided biopsies or during neurosurgical interventions (1, 17). Numerous tissue ablation techniques have been developed using MR imaging guidance for probe placement and monitoring of the therapy. Laser-induced thermotherapy is based on heat transfer between an optical fiber and the surrounding tissue, resulting in coagulative necrosis of the targeted lesion. In several clinical studies, it has been shown to be sufficient for therapy of cerebral gliomas (3, 18). Another attempt of focal hyperthermal therapy is RF thermal ablation. It depends on transfer of electrical energy to tissue because of the electrical resistance of the targeted tissue. RF ablation has been used during neurosurgical interventions for a long time (19) and has been successfully combined with MR imaging guidance in the treatment of brain tumors (2). With both techniques, laser and RF ablation, temperature sensitivity of MR imaging is used to image the heating process during ablation. The T1 relaxation time of tissue depends on temperature, resulting in a decrease of T1 relaxation time during heating. Because these changes of T1 take place in a small range of gray scale on MR images, color-encoded temperature mapping (including dedicated software and hardware) is necessary to image the area of hyperthermia more precisely.

Image-guided cryotherapy of the brain has been performed in animal experiments only. Moser et al (20) performed cryotherapy under CT control in the brain of four dogs. Using a metallic 4.76-mm-diameter cryoprobe, the maximum ice ball diameters were 2 cm. Because of the metal content of the probe, the image quality was poor if the section was selected through the cryoprobe. Thus, images with sufficient quality could be obtained only if the section was set beneath the probe tip, preventing a complete imaging of the ice formation. On CT scans, the frozen tissue appeared as a hypointense sphere with sharp delineation to the unfrozen brain tissue. Quigley et al (21) performed sonography-guided cryotherapy in six dogs after bilateral craniotomy, allowing continuous sonographic monitoring. Cryotherapy resulted in lesion diameters of $\leq$1.5 cm. The appearance of the frozen tissue on sonograms was a hyperechoic sickle, with sound shadow posterior to the interface between unfrozen and frozen tissue.

The first MR imaging–guided cryotherapy of the brain was performed by Gilbert et al (6). They performed cryotherapy in 11 rabbits after craniotomy

by using an experimental surface cryoprobe. The ice formation (including cortex, skull, and skin) appeared signal-free on T1-weighted spin-echo and gradient-echo sequences. To the best of our knowledge, this study describes the first minimally invasive interstitial cryotherapy of the brain that was planned and monitored by using MR imaging alone. Because there were no MR imaging–compatible cryoprobes commercially available at the beginning of this study, a custom-made cryoprobe was built of glass. This probe caused no artifacts on MR images and only few beam-hardening artifacts on CT scans. Its cooling power allowed the creation of ice balls 12.5 mm in diameter in the vital brain. Including vacuum insulation, which has been shown to be effective in this study, the outer diameter did not exceed 2.7 mm. Thus, significant damage of neurogen structures along the puncture channel could be avoided. Although glass is too brittle for clinical application, this probe permitted initial experimental experiences in MR imaging–guided cryotherapy. All of the tested sequences and CT permitted sufficient temporal resolution during the 1.5 minutes from starting freezing until achieving the maximum ice ball size. The best contrast between the frozen and unfrozen tissue was achieved using the T1-weighted fast field echo sequence (imaging duration, 4 s per image). Moreover, this sequence allowed a good differentiation between gray and white matter. The interactive T1-weighted radial fast field echo sequence was comparable with the T1-weighted fast field echo sequence in ice:tissue contrast. This sequence is characterized by a time frame of $\leq$25 images per second, resulting in real-time imaging. Furthermore, the interactive capabilities of this sequence allowed the operator to change the image plane and angulation, section thickness, and flip angle during imaging. This was very helpful in imaging the ice formation in all directions, because it permitted not only standard projections but also ''walking through'' the ice ball. The third sequence tested was the T2-weighted ultrafast LoLo sequence, characterized by a true T2-weighted contrast with sufficient imaging of the CSF and the resulting edema of the previously frozen tissue. In all sequences, the ice was imaged as a signal-free, sharply delineated spherical formation with excellent contrast to the surrounding, unfrozen brain parenchyma. The ice:tissue contrast on MR images, ranging from 91% (T1-weighted fast field echo) to 81% (LoLo), was statistically significantly better when compared with that of CT scans (58% $\pm$ 11.2%). Although the ice was spherically shaped and sharply delineated on the CT scans, the soft-tissue contrast was poor compared with that on the MR images. For a future clinical application of cerebral cryotherapy, it must be concluded that monitoring by MR imaging is superior to monitoring by CT. Because radial fast field echo and LoLo sequences are not yet available options on all clinical imagers, the T1-weighted fast field echo will probably be preferable because of its robustness and its excellent ice:tissue contrast. The LoLo sequence will offer a better delineation of edema (because of tumor or cryogenic lesions), even without application of contrast agents.

The MR imaging follow-up of the cryogenic lesions showed a typical appearance, which was concordant in all animals. Immediately after thawing, there was a zone of edema corresponding to the size of the ice formation. The appearance of the lesion on contrast-enhanced images immediately after cryotherapy corresponded very well to the lesion size on MR images obtained 14 days after freezing. The increase of the lesion size in diameter at 3 and (less pronounced) 7 days after cryotherapy can be explained by the edematous reaction of the lesion and the surrounding brain parenchyma. As known from ultrastructural freezing experiments (22, 23), crystallization of water occurs in the intra- and extracellular spaces. Whereas intracellular ice occurs only during very high cooling rates and causes immediate damage of the cellular components, extracellular ice causes dehydration of the surrounding cells. Because of the resulting osmotic shift, small vessels may expand to twice their normal diameter. This destroys the structural integrity of the vascular system and deprives those cells that have escaped direct cryotherapy damage of their blood supply. In addition, the endothelial layer of the capillaries begins to leak and the amount of interstitial fluid thus increases.

As observed on follow-up control MR images, these changes seem to be most pronounced 3 days after cryotherapy. The decrease of lesion size 7 days after cryotherapy seems to be a result of disappearing edema and beginning removal of the necrotic tissue. Fourteen days after cryotherapy, these mechanisms continue and the scarring process begins. The histologic findings of this study are comparable with those of other studies (6, 20, 21, 24). The previously frozen tissue was completely necrotic and sharply delineated to the unfrozen and viable brain tissue by a transition zone of approximately 200 μm. The brain tissue outside of the cryolesion was shown to be unaffected by both macroscopic and histologic examination. That the differences in the diameters of the cryolesions 7 and 14 days after cryotherapy were clearly seen on MR images but less clearly in histologic specimens warrants further discussion. First, the brain shrinks after formalin fixation by a factor of approximately 1.14. Considering that the lesions were located excentrically within the brain and that some included the cortex and others did not, an uncertain difference of tissue shrinkage can be assumed. Second, the amount of edema that was seen on MR images obtained 7 days after cryotherapy was more extended than on MR images obtained 14 days after intervention. Because all histologic specimens were dehydrated by different concentrations of ethanol before undergoing hematoxylin and eosin staining,

the differences in lesions size, which are caused by edema, can be equalized.

Conclusion

The combination of modern fast and ultrafast MR imaging sequences with minimally invasive cryotherapy permits precise planning and monitoring of the targeted lesion size during therapy. The clinical application of this new technique seems to be possible in the near future, if MR imaging–compatible cryoprobes with sufficient cooling capacity become available. The spectrum of indications for MR imaging–guided cryotherapy is wide and includes ablation of dysfunctional foci and brain tumors (25–28). Because monitoring of cryotherapy with MR imaging needs no dedicated temperature-sensitive sequences or additional hardware, it may be performed using a wide variety of imagers that are suited for interventional procedures. In general, all fast MR imaging sequences are useful for imaging frozen tissue. An advantage of fast T2-weighted pulse sequences may be good and continuous delineation of tumor due to the surrounding edema without additional contrast medium administration. However, fast T1-weighted gradient-echo sequences permit a better contrast between the frozen and unfrozen brain tissue.

References

1. Bernays R, Kollias S, Romanowski BJ. **Real-time MR-guided neurosurgical interventions.** In: Debatin JF, Adam G, eds. I*nterventional Magnetic Resonance Imaging.* Berlin: Springer;1998: 151–155
2. Anzai Y, Lufkin R, DeSalles A, Hamilton DR, Farahani K, Black KL. **Preliminary experience with MR-guided thermal ablation of brain tumors.** *AJNR Am J Neuroradiol* 1995;16:39–48
3. Kahn T, Bettag M, Ulrich F, et al. **MRI-guided laser-induced interstitial thermotherapy of cerebral neoplasms.** *J Comput Assist Tomogr* 1994;18:519–532
4. Heimburger RF. **Ultrasound augmentation of central nervous system tumor therapy.** *Indiana Med* 1985;78:469–476
5. Cline HE, Schenck JF, Hynynen K, Watkins RD, Souza SP, Jolesz FA. **MR-guided focused ultrasound surgery.** *J Comput Assist Tomogr* 1992;16:956–965
6. Gilbert JC, Rubinsky B, Roos MS, Wong STS, Brennan KM. **MRI-monitored cryosurgery in the rabbit brain.** *Magn Reson Imaging* 1993;11:1155–1164
7. Isoda H. **Sequential MRI and CT monitoring in cryosurgery: an experimental study in rats [in Japanese].** *Nippon Igaku Hoshasen Gakkai Zasshi* 1989;49:1499–1508
8. Matsumoto R, Oshio K, Jolesz FA. **Monitoring of laser and freezing-induced ablation in the liver with T1-weighted MR imaging.** *J Magn Reson Imaging* 1992;2:555–562
9. Tacke J, Speetzen R, Heschel I, Hunter DW, Rau G, Günther RW. **Imaging of interstitial cryotherapy: an in-vitro comparison of US, CT and MRI.** *Cryobiology* 1999;38:250–259
10. Tacke J, Adam G, Speetzen R, et al. **MR-guided interstitial cryotherapy of the liver with a novel, nitrogen-cooled cryoprobe.** *Magn Reson Med* 1998;39:354–360
11. Gilbert JC, Yu K, Fell S, Hricak H, Brennan KM, Kurhanewicz J. **MRI evaluation of tissue damage immediately after cryosurgical freezing of canine prostate.** Presented at the 6th Scientific Meeting of the ISMRM, Sydney, April 18–24, 1998
12. Tacke J, Speetzen R, Schorn R, et al. **Experimental MR-guided cryotherapy of the brain with almost real-time imaging by radial k-space scanning [in German].** *Fortschr Röntgenstr* 1999; 170:214–217
13. van Vaals JJ, van Yperen GH, de Boer RW: **Real-time MR imaging using the LoLo (Local Look) method for interactive and interventional MR at 0.5T and 1.5T.** *SMR Book of Abstracts.* vol 1.1994:412
14. Rasche V, de Boer RW, Holz D, Proksa R. **Continuous radial data acquisition for dynamic MRI.** *Magn Reson Med* 1995;34: 754–761
15. Riederer SJ, Tasciyan T, Farzaneh F, Lee JN, Wright RC, Herfkens RJ. **MR fluoroscopy: technical feasibility.** *Magn Reson Med* 1988;8:1–15
16. Remmele, W. **Besondere Hinweise zur Formalinfixierung.** In: Remmele W, ed. *Pathologie.* Berlin: Springer;1999:30–34
17. Tronnier VM, Wirtz CR, Knauth M, et al. **Intraoperative diagnostic and interventional magnetic resonance imaging in neurosurgery.** *Neurosurgery* 1997;40:891–900
18. Reimer P, Bremer C, Horch C, Morgenroth C, Allkemper T, Schuierer G. **MR-monitored LITT as a palliative concept in patients with high grade gliomas: preliminary clinical experience.** *J Magn Reson Imgaging* 1998;8:240–244
19. Aronow S. **The use of radio-frequency power in making lesions in the brain.** *J Neurosurg* 1960;17:431–438
20. Moser RP, Abbott IR, Stephens CL, Lee YY. **Computerized tomographic imaging of cryosurgical ice ball formation in brain.** *Cryobiology* 1987;24:368–375
21. Quigley MR, Loesch DV, Shih T, Marquardt M, Lupetin A, Maroon JC. **Intracranial cryosurgery in a canine model: a pilot study.** *Surg Neurol* 1992;38:101–105
22. Rubinsky B, Lee CY, Bastacky J, Hayes TL. **The mechanism of freezing in biological tissue: the liver.** *Cryo-Letters* 1987;8:379–381
23. Giampapa, VC, Changyul OH, Aufses AK. **The vascular effect of cold injury.** *Cryobiology* 1981;18:49–54
24. Miyazaki Y, Erwin FR, Siegfried J. **Localized cooling in the central nervous system: part II. histopathologic results.** *Arch Neurol* 1963;9:392–399
25. Cooper IS. **A cryogenic method for physiologic inhibition and production of lesions in the brain.** *J Neurosurg* 1962;19:853–858
26. Cooper IS, Stellar A. **Cryogenic freezing of brain tumors for excision or destruction in situ.** *J Neurosurg* 1963;20:921–930
27. Maroon JC, Onik G, Quigley MR, Bailes JE, Wilberger JE, Kennerdell JS. **Cryosurgery re-visited for the removal and destruction of brain, spinal and orbital tumours.** *Neurol Res* 1992;14: 294–302
28. Rand RW. **The role of cryosurgery and MRI for Parkinon's disease.** Presented at the 9th World Congress of Cryosurgery, Paris, May 31–June 3, 1995